UC San Diego
UC San Diego Previously Published Works

Title

Structure and Function of Iron-Loaded Synthetic Melanin.

Permalink

https://escholarship.org/uc/item/93s3j153

Journal

ACS Nano, 10(11)

Authors

Li, Yiwen

Xie, Yijun

Wang, Zhao

et al.

Publication Date

2016-11-22

DOI

10.1021/acsnano.6b05502

Peer reviewed

Structure and Function of Iron-Loaded Synthetic Melanin

Yiwen Li[†,‡,¶], **Yijun Xie**[‡,§,¶], **Zhao Wang**[‡,¶], **Nanzhi Zang**[‡,§], **Fabio Carniato**[‖], **Yuran Huang**[‡,§], **Christopher M. Andolina**[⊥], **Lucas R. Parent**[‡], **Treffly B. Ditri**[‡], **Eric D. Walter**[#], **Mauro Botta**[‖], **Jeffrey D. Rinehart**[‡,*], and **Nathan C. Gianneschi**[‡,§,*]

[†]College of Polymer Science and Engineering, State Key Laboratory of Polymer Materials Engineering, Sichuan University, Chengdu 610065, China

[‡]Department of Chemistry and Biochemistry, University of California, San Diego, 9500 Gilman Drive, La Jolla, California 92093, United States

[§]Materials Science and Engineering Program, University of California, San Diego, 9500 Gilman Drive, La Jolla, California 92093, United States

[‖]Dipartimento di Scienze e Innovazione Tecnologica, Università del Piemonte Orientale "A. Avogadro", Alessandria, Italy

[⊥]Department of Chemistry, University of Pittsburgh, 4200 Fifth Avenue, Pittsburgh, Pennsylvania 15260, United States

[#]Institute for Integrated Catalysis, and Environmental Molecular Sciences Laboratory, Pacific Northwest National Laboratory, Richland, Washington 99354, United States

Abstract

We describe a synthetic method for increasing and controlling the iron loading of synthetic melanin nanoparticles and use the resulting materials to perform a systematic quantitative investigation on their structure–property relationship. A comprehensive analysis by magnetometry, electron paramagnetic resonance, and nuclear magnetic relaxation dispersion reveals the complexities of their magnetic behavior and how these intraparticle magnetic interactions manifest in useful material properties such as their performance as MRI contrast agents. This analysis allows predictions of the optimal iron loading through a quantitative modeling of antiferromagnetic coupling that arises from proximal iron ions. This study provides a detailed understanding of this complex class of synthetic biomaterials and gives insight into interactions and structures prevalent in naturally occurring melanins.

Graphical abstract

[*]**Corresponding Authors**. jrinehart@ucsd.edu. ngianneschi@ucsd.edu.
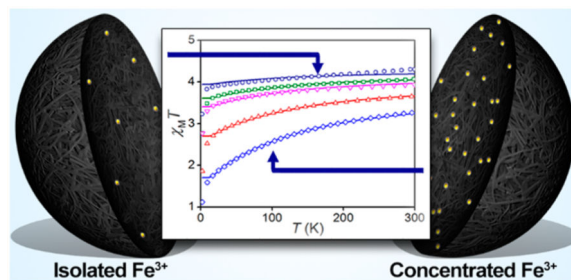[¶]Y. Li, Y. Xie, and Z. Wang contributed equally to this work.

The authors declare no competing financial interest.

The natural function and structure inherent to the biomaterial melanin have sparked interest in its utility across a broad range of biomedical applications.[1] Recent work has shown that through the self-oxidation polymerization of dopamine under alkaline conditions, synthetic mimics of natural melanin, with similar chemical structure as well as physical and biological properties, can be achieved.[2,3] These polydopamine (PDA)-based synthetic nanoparticles retain many of the desirable properties of natural melanin and have been studied for use in catalysis,[4] free radical quenching,[2,3] inkjet printing,[5,6] photothermal therapy,[7,8] and structural coloration.[9,10] Many of these applications rely on the strong binding affinity of catechol-based functional groups, allowing robust coordination of various transition metals.[11–13] Despite the proliferation of work in this area, the complex, amorphous nature of the material necessitates a multitechnique approach to elucidate the physical, electronic, and magnetic structure.[3] Herein, we employ a host of complementary techniques to define the properties of synthetic melanin nanoparticles (SMNPs) prepared by a synthetic route that, critically, provides tunability of the Fe(III) content. A similar synthetic method to ours has been described very recently in a report focusing on morphological control in battery applications.[14] Our goal to study the evolution of magnetic and spectroscopic properties led us to focus on a synthetic strategy that provides particles that incorporate a wide range of concentrations of high-spin Fe(III).

Synthetic melanin-based materials are of particular interest as MRI contrast agents due to their excellent biocompatibility and ability to coordinate isolated paramagnetic metal centers.[15,16] The catechol-functionalized network of the nanoparticle acts as a scaffold for chelation of paramagnetic metal ions, leading to T_1-weighted MRI contrast. Although a number of studies have been published on such materials, questions remain about the origin and the path to optimization of the MRI contrast.[3] Our approach initially involved the development of synthetic methods to achieve high metal loadings, as T_1-weighted MRI contrast should scale linearly with the number of isolated paramagnetic centers. The obvious method for preparation of SMNP MRI contrast agents is to expose the already-formed SMNP to a solution containing Fe(III) cations, an approach we term the postdoping synthetic strategy (Scheme 1a). The postdoping synthetic strategy is convenient and allows for the complexation of a variety of cations.[24] However, this approach generally limits the metal loading efficiency, which in our hands results in less than 1% iron by mass.[15]

Although this situation can be improved somewhat by decreasing the surface-to-volume ratio of SMNPs,[15] achieving ultrahigh, tunable Fe(III) loadings (*i.e.*, >5%) for optimizing and studying the magnetic properties and resulting SMNP-based MRI contrast has remained elusive.

Another important question is how water relaxation can occur in a system with strongly chelating catechol units interacting with Fe(III). Considerable insight into the coordination environment of catechol-based materials in general has been gained through electron paramagnetic resonance (EPR) and Mössbauer spectroscopies.[17–21] EPR in particular has given a wealth of data regarding the presence or absence of radical electrons and trace metal ions. However, systems with higher quantities of Fe(III) are difficult to analyze by these techniques due to nonuniform coordination environments and interior magnetic interactions. By contrast, magnetometry excels at the analysis of higher magnetic concentrations and can also reveal details of the local anisotropy and coupling interactions that are vital to understanding the magnetic nature of highly doped materials. Notably, although a variety of analytical methods have been individually employed in characterizing natural melanins,[22–24] a thorough analysis by combined methods allows us to exploit the specific strengths of each technique to understand the coordination environment and magnetic interactions of synthetic mimics of melanin and, in the future, potentially the natural biomaterial itself in all its various forms.

RESULTS AND DISCUSSION

Synthesis and Characterization of SMNPs by Electron Microscopy

To prepare a series of SMNP contrast agents with a broad range of Fe(III) loadings for systematic structure– property relationship analysis, the development of a general Fe(III)-doping strategy to achieve >5% loading was required. This was accomplished through the use of a prepolymerization doping strategy, which employs a mixture of Fe(III)-(dopamine)$_3$[25] and free dopamine as the precursors for the formation of Fe(III)-chelated SMNPs (Scheme 1b). During the polymerization process, in the presence of Tris (Table S1),[26] Fe(III) can be continuously incorporated into the SMNP as it forms, allowing tunable, high doping levels of metal ions inside the particle. We have employed this prepolymerization doping strategy (SMNP-i (i = 2–5), Table S1) and the standard postdoping strategy (SMNP-1) to synthesize a series of Fe(III)-doped SMNPs with various Fe(III) concentrations (Table S2). Note that Fe(III) loading in SMNP-5 could even reach 10.26%. Additionally, our prepolymerization doping one-pot strategy features several advantages over the postdoping synthetic strategy including efficiency of synthesis, leading to generally higher yield reactions due to less purification work.

All SMNPs were characterized by transmission electron microscopy (TEM) (Figure S1) and scanning electron microscopy (SEM) (Figure S2) to quantify their size and uniformity. The combination of TEM, cryo-TEM, and SEM (Figures 1, S1, S2) shows spherical nanoparticles with diameters in the range of 140 to 250 nm (Table S2). The presence of metal inside the nanoparticles was evident in the high contrast they exhibit when observed *via* high-angle annular dark field (HAADF)-STEM and bright-field scanning transmission electron microscopy (BF-STEM) (Figure S3). Selected area HAADF-STEM coupled with

energy-dispersive X-ray spectroscopy (EDS) further confirms the presence of Fe(III) ions localized in the nanoparticles (Figure S4). The EDS profiles suggest that the content of iron in the testing areas of SMNP-4 was significantly higher than that on the grid surface background, which is in good agreement with the elemental mapping analysis results (Figure 1). Together, these results strongly suggest that SMNP-i ($i = 0$–5) are morphologically similar at the nanoscale, and hence, we expect them to differ only in the average number of unpaired spins imparted by the Fe(III) ion content.

Characterization of SMNPs by NMRD and MR Imaging Analysis

Additional unpaired spins present in the higher Fe(III)-loaded samples should have a strong effect on the relaxometry of proximal solvent protons. This effect, the source of T_1 contrast enhanced MRI, was probed through measurement of the longitudinal water proton relaxation rates (R_1) as a function of applied magnetic field for all SMNP samples. ^{1}H nuclear magnetic relaxation dispersion (NMRD) allows an accurate determination of the field dependence of R_1 that arises from the magnetic interaction between the metal centers and the solvent.[27,28] This takes place either through chemical exchange between the bound water and the bulk water molecules (inner sphere) or through a long-distance interaction with outer-sphere water molecules that rapidly diffuse near the paramagnetic centers (outer sphere). Shown in Figure 2 are the ^{1}H NMRD profiles of SMNP-i ($i = 1$–5) measured at 298 K in the range 2.3 mT to 1.6 T. The data are expressed in terms of relaxivity, r_{1p}, which is defined as the relaxation rate enhancement induced by 1 mmol/L of the paramagnetic ion. With the exception of the lowest Fe(III)-loading sample, the NMRD profiles of the SMNPs show a similar shape characterized by a low-field plateau (*ca.* 0.1–1 MHz), followed by a dispersion around ~2–4 MHz and a relatively small increase at frequencies above *ca.* 30 MHz. The single dispersion displayed at about 3 MHz corresponds to a correlation time $\tau_C \approx 9 \times 10^{-11}$ s. Due to the slow rotational dynamics (long τ_R values) of paramagnetic centers in these nanoparticles, we attribute this correlation time to the electronic relaxation time τ_S, which has been reported to fall in the range 10^{-11} to 10^{-9} s.[29] The clear increase of r_{1p} above *ca.* 30 MHz makes it evident that (1) τ_S is field dependent and (2) τ_S represents a predominant factor in the determination of τ_C. This behavior resembles that reported by Bertini *et al.* in the case of the ^{1}H NMRD profiles of Fe(III) aqua ions in different glycerol–water mixtures.[30] By increasing the viscosity, the relative contribution of τ_R to τ_C with respect to τ_S decreases and the relaxivity in the high-field region increases. The NMRD profile of the iron-binding glycoprotein transferrin shows a similar general trend, although with a more pronounced decrease of r_{1p} with frequency in analogy with that observed for SMNP-1.[31] All these features suggest the presence of one or more water molecules bound to the metal centers ($q \ge 1$), at least for a certain population of the Fe(III) centers.

The shape and amplitude of the NMRD profiles suggest various contributions to the relaxivity. The relative complexity of the shape of the profiles reflects the distribution of different populations of species with different coordination environments and thus magnetic properties. The outer-sphere contribution to relaxivity, predominant in the case of triscatechol-Fe(III) species ($q = 0$), is generally rather small and can be estimated at approximately 1–2 mM^{-1} s^{-1}.[32] When water is bound to an Fe(III) cation in a macromolecule, the long exchange lifetime often represents a limiting effect on relaxivity.

However, as shown by the case of fluoromethemoglobin,[33] high relaxivity values can be associated with fast exchanging water molecules H-bonded to hydroxide ligands on or next to Fe(III) ions (second-sphere contribution).[33] The dominant role of this mechanism has recently been discussed in the case of polycatechol nanoparticles.[34] All these contributions, with different weights, are likely to play a role in determining the relaxation behavior of these SMNPs.

Since each SMNP can contain many chelated Fe(III) ions, it is interesting to consider the per particle relaxivity ($r_{1p(particle)}$) to describe the local concentration necessary to achieve the desirable T_1 MR imaging contrast under different magnetic fields.[35] Figure 2b shows the calculated $r_{1p(particle)}$ of each SMNP. Interestingly, the plots of $r_{1p(particle)}$ and $r_{1p(Fe(III))}$ show different trends (*i.e.*, see Figure S5 for $r_{1p(particle)}$ and $r_{1p(Fe(III))}$ results of SMNPs at 20 MHz). Whereas $r_{1p(Fe(III))}$ reveals a diminishing return for additional Fe(III), the plot of $r_{1p(particle)}$ shows there is an upper limiting doping level (*i.e.*, SMNP-4) after which the ^{1}H NMRD shows a decrease in relaxivity over all frequencies. These data lead to the counterintuitive result that highly paramagnetically doped particles are inferior to those doped with lower levels of Fe(III) ions. The origin of this effect will be discussed in subsequent sections.

The long-term stability of any MRI contrast agent in biological fluids is a prerequisite to ensure their *in vitro* and *in vivo* MR imaging performance. Similar to the reported SMNP-1 chelating platform,[36] SMNP-*i* (*i* = 2–5), synthesized *via* the predoping strategy demonstrate high stabilities (Figure S6). Notably, the Fe(III) content of each SMNP remains at approximately 100% of the original value after 1 week of exposure to PBS. Additionally, the long-term MRI signal-enhancing capability of Fe(III)-chelated nanoparticles was tested in a Bruker 7.0 T magnet in different media including water, PBS buffer, fetal bovine serum (FBS), and Dulbecco's modified Eagle medium (DMEM). SMNP-1 and SMNP-4 were selected as samples in this study with SMNP-0 employed as the control. SMNP-1 and SMNP-4 exhibited signal enhancement in T_1-weighted MR images in different media (Figure 3). After 5 days of incubation with serum and cell culture medium, the MR images for both SMNP-1 and SMNP-4 samples did not lose intensity, suggesting long-term stability of SMNP agents in biological fluids. Additionally, at the same particle concentration (1.3 mg/mL was used in this study), MR images for SMNP-4 are much brighter than those of SMNP-1 under identical conditions, in good agreement with shorter T_1 relaxation (Figure 3). All observations indicate that SMNP-4 enables the best *in vitro* MRI performance at a fixed particle concentration. Subsequently, a systematic study was performed to investigate the long-term MRI contrast-enhancing capability of all SMNP-*i* (*i* = 1–5) samples in different media including water and cell culture media (*i.e.*, 90% DMEM with 10% FBS). It was observed that freshly prepared SMNP-*i* (*i* = 1–5) show similar relaxivity in cell culture medium compared with water (Figure S7 and Table S3). In addition, we note that after 5 days of incubation with cell culture medium, the relaxivity values for all SMNP samples do not decrease, confirming the materials are promising in terms of long-term stability of SMNP MRI agents in biological fluids.

Magnetochemical Analysis of SMNPs

Several intriguing questions arise from the relaxivity data: (1) Is the T_1 contrast arising from an inner-sphere binding event, despite the propensity for catechol to form strong tris-chelates in neutral and basic solutions? (2) Why is there not a linear increase in the relaxivity response with additional Fe(III) cations, as would be expected for T_1 contrast? To address these questions directly, we turned to techniques that are sensitive to the local spin states as well as the ensemble properties of the magnetic structure.

EPR spectra of frozen solutions were collected at 125 K (Figure 4a), providing significant information regarding the distribution of radicals within Fe(III)-loaded SMNPs.[37] The characteristic spectrum of the persistent radical, which is a hallmark of all melanins, is visible in samples with less than 2% iron. As reported, paramagnetic metals can reduce the amplitude of this peak,[38] completely suppressing it at high loadings. All iron-containing samples show a peak at 1600 G ($g = 4.3$), which is attributed to high-spin Fe(III) in sites of low symmetry of tetrahedral or octahedral coordination.[23] The width of this peak increases with increased iron loading due to spin–spin dipolar coupling.[39] From these data, we determined the change in the full width at half-maximum as a function of total iron, with the linear progression suggesting that the iron loading is evenly distributed in a 3-D matrix of sites, as opposed to either lower dimensional arrangements or clusters (Figure S8).[40]

At the highest iron loading levels, a very broad spectrum centered near $g = 2$ is evident. In many systems, a spectrum of this form is due to superparamagnetic or ferromagnetic particles. Therefore, the spectrum of SMNP-5 was recorded over a wide range of temperatures to explore the magnetic properties of this species (Figure 4b).[41] However, unlike a ferromagnetic material, which would have a constant intensity, or a superparamagnetic material, which would have spectra that would broaden and shift to lower field as the temperature is lowered, the spectra increase in amplitude as the temperature is lowered to 20 K, but then sharply diminish in amplitude at 3.5 K. This behavior indicates the occurrence of a more complex magnetic behavior that gains in strength with increasing Fe(III) loading.

To elucidate the origin of this alteration in the magnetic structure at high Fe(III) cation concentrations, the temperature dependence of the SMNP magnetic susceptibility was investigated by superconducting quantum interference device (SQUID) magnetometry (Figure 5). The lowest Fe-loading sample (SMNP-1) was expected to largely exhibit characteristics of the isolated octahedral high-spin d^5 configuration of Fe(III) ($S = 5/2$) as demonstrated by the EPR data. Indeed, the product of magnetic susceptibility and temperature per mole Fe ($\chi_M T$) at 300 K approaches the expected spin-only value of 4.375 emu K cm^{-3} mol^{-1} for a purely Fe(III)-containing sample. This close agreement precludes the possibility of significant Fe(II) and low-spin Fe(III) populations, as they would lead to significant alterations in the $\chi_M T$ value. As temperature is decreased from 300 K, the effects of antiferromagnetic Fe(III)–Fe(III) interactions begin to manifest in the $\chi_M T$ data. For SMNP-1 with only 0.46% Fe(III) loading, the majority of Fe(III) centers are sufficiently isolated so as to display their full, uncoupled moment. However, a nonnegligible subset of Fe(III) are close to other Fe(III) sites and thus display antiferromagnetic interactions that lower the overall $\chi_M T$ value. As we increase the Fe(III) concentration up to 10.26%

(SMNP-5), deviations from the spin-only expectation become more drastic, leading to a drop of more than 20% in the $\chi^M T$ product at room temperature.

We find that a relatively simple model, incorporating an isotropic g value and magnetic coupling constant (J_{Fe-Fe}), is able to satisfactorily explain the coupling behavior of Fe(III). In this model, we need only consider two general types of Fe(III) centers: magnetically isolated Fe(III) and magnetically coupled Fe(III). This assumption is based on the weak superexchange pathway that the catechol functional groups of PDA provide. Indeed, model molecular Fe(III) catecholate dinuclear complexes display coupling constants of less than 30 cm^{-1}, even when only separated by a single catecholate oxygen.[42–44] The ratio between the uncoupled and coupled Fe(III) subsets is fitted along with an isotropic g and J_{Fe-Fe} value by simultaneous global fitting of all susceptibility data. Uncoupled Fe(III) is modeled as an ideal paramagnetic $S = 5/2$ Fe(III), whereas coupled Fe(III) is modeled through an HDVV Hamiltonian (eq 1) where $\hat{S}_1$ and $\hat{S}_2$ are spin operators for equivalent interacting spins. Although most natural and synthetic melanin systems have been shown to possess some radical electron character,[3,45,46] we do not find it necessary to include radical electrons in our model. This is corroborated by measuring magnetic susceptibility of equivalently synthesized pure melanin nanoparticles (SMNP-0) without Fe(III) loading, which shows a negligible paramagnetic moment across all temperatures (Figure S9). This does not imply that no radical population is present, only that it is necessarily low enough to be inconsequential to the overall magnetism. In fact, EPR spectra (Figure 4) confirm the presence of organic radicals in SMNP-0 and SMNP-1

$$\hat{H} = -2J_{Fe-Fe}\hat{S}_1 \cdot \hat{S}_2 \quad (1)$$

The fitting results reveal antiferromagnetic coupling ($g = 2.05 \pm 0.04$; $J_{Fe-Fe} = -24.8 \pm 2.7$ cm^{-1}) that corresponds well to molecular Fe-catechol systems.[42,47,48] Of particular note is that at very high Fe(III) loadings (SMNP-5) over half of the Fe(III) is now involved in magnetic coupling interactions, leading to a significant drop in the moment even under ambient temperature conditions. This behavior tracks well with the low $r_{1p(Fe(III))}$ of the SMNP-5 sample (Figure 2a). From the view of MRI contrast agents, this antiferromagnetic coupling tempers the advantage of high loading because of the significant reduction in room-temperature moment per iron center compared with less concentrated Fe(III) samples. Additionally, the magnetically coupled Fe(III)–Fe(III) interactions can alter the nature of the relaxation, shifting of the SMNP toward T_2-weighted agents at high concentrations. These factors indicate that there will be an optimal Fe(III) concentration. This relatively strong coupling also indicates that short Fe(III)–Fe(III) ligand-based bridges can exist within the PDA structure, an intriguing result considering that mononuclear molecular Fe(III)-catechol exists as a mixture of bis- and tris-catechol-Fe(III) species at our synthetic conditions (pH ~9).[49] Since a tris-catechol binding mode would inhibit the formation of effective superexchange bridges, the strength of coupling we observe may indicate a low catechol coordination number for Fe(III) within the SMNP. If in fact, the PDA structure is limiting the catechol coordination, this opens the exciting possibility that water is able to directly

bind to Fe(III) centers or interact with hydroxides directly bound to Fe(III) centers, thus explaining the strong MRI contrast observed for Fe(III)-coordinated synthetic melanin.[15]

Further evidence of limited Fe-catechol bonding was obtained by scrutinizing the deviations from ideal paramagnetic behavior observed at very low temperature. These deviations are caused by magnetic anisotropy induced by a low-symmetry coordination environment as well as Zeeman splitting due to the applied field. To isolate the effects of the magnetic anisotropy, we performed a series of low-temperature, variable-field measurements for SMNP-1, which has the lowest amount of coupled Fe(III) (Figure 6a). We focus on SMNP-1 because 90% of the Fe(III) is in the uncoupled state, and the magnetic influence of the remaining 10% is minimized due to its relative isolation in the antiferromagnetically coupled ($S = 0$) state at low temperature. Under these approximations, the molar magnetization values in Figure 6a are solely due to uncoupled Fe(III) ions. By fitting to an axially anisotropic Hamiltonian (eq 2) using the MagProp module of DAVE 2.3 (Figure 6),[50] a small but non-negligible axial anisotropy is determined to be present ($D = 0.88 \pm 0.29$). Interestingly, this value corresponds to that observed for monocatechol-bound Fe(III) in acidic aqueous solution ($D = 0.82$), but is significantly higher than the bis- and tris-catechol-bound Fe(III) ($D = 0.42$ and $D = 0.32$, respectively).[19] High Fe(III) concentration samples (SMNP-2 through SMNP-5) gave similar results although with less satisfactory error values due to the added complication of large contributions from coupled Fe(III) (Figure S10).

$$\hat{H} = g\mu_{\mathrm{B}}\hat{S} \cdot B + D\left[\hat{S}_{\mathrm{z}}^2 - \frac{S(S+1)}{3}\right] \quad (2)$$

The magnetic evidence strongly suggests that despite the high concentration of catechol in SMNP materials and pH values during synthesis that should initially favor a tris-catechol binding mode, Fe(III) is largely coordinated as the monocatechol in the final product. As this result was somewhat counterintuitive, UV–vis spectroscopy was employed to corroborate our magnetic analysis. Figure 6b shows that both high (SMNP-5) and low (SMNP-3) Fe(III) loadings exhibit a broad peak at 710 nm, which is indicative of monocatechol-Fe(III) complexes.[18,49,51] In stark contrast to previously studied free Fe(III) catechol systems,[49,51] this peak persists even at very basic pH values for 24 h with no indication of bis- or triscatechol formation (Figure S11). These data suggest that melanin-based MRI contrast agents may allow for water exchange through an "inner-sphere" T_1 relaxation, even for Fe(III) embedded within the nanoparticle.[15,52]

From the combination of magnetometry and magnetic spectroscopy (EPR) we can conclude that isolated paramagnetic iron centers exist throughout the SMNPs. At higher concentrations, the Fe(III) does not form oxide particles that would show ordered magnetic behavior but does form weak antiferromagnetic superexchange interactions that effectively cancel out a significant portion of the 300 K magnetization. Additionally, the high magnetic anisotropy indicates a low-symmetry environment that is not consistent with tris-catechol coordination of Fe(III); thus the superexchange is likely mediated by diamagnetic bridging ligands and not the polymer backbone.

CONCLUSIONS

In summary, a technique for accessing SMNPs with tunable iron loadings has offered opportunity for their magneto-structural analysis through the combined utilization of SQUID magnetometry, EPR, and ^{1}H $1/T_1$ NMRD. The results presented herein also suggest a number of avenues for optimizing MRI contrast in synthetic melanin nanoparticles: (1) Because high Fe(III) loading leads to a lowering of the moment per Fe(III) center, decreasing coupling between paramagnetic centers would necessarily increase the magnetic moment at higher loadings. This, in turn, could increase the T_1 relaxation rate of surrounding water protons due to the presence of more unpaired electron spins. This could be achieved by a number of synthetic approaches including the expansion of the polymer backbone to increase the distance between Fe(III) binding sites or incorporating higher spin, weaker coupling ions. (2) Alternatively, the antiferromagnetic coupling could be disrupted through the creation of an alternate, small-spin magnetic coupling channel between Fe(III) and an organic radical electron or $S = 1/2$ transition metal centers such as Cu(II). Thus, antiferromagnetic coupling would result in a net $S = 2$ state even at very high ion loadings, preventing the decrease of magnetic moment. Particles of this type would, however, likely exhibit T_2-weighted contrast similar to other highly coupled particle systems such as magnetite. (3) Since monocatechol coordination is likely the result of steric hindrance created by the rigid cross-linked polymer backbone, modulating this steric hindrance may create better intraparticle channels for replacing water at Fe(III) binding sites while still preventing multicatechol binding. Alternatively, the polymer backbone can be modified to electronically enhance the local water exchange rate at Fe(III) sites.

With the current interest in metal-doped melanin and polycatechol-based nanomaterials, a fundamental understanding of the electronic and magnetic structure is vital. The conclusions herein offer potential synthetic targets that could lead to more directed syntheses of effective contrast agents. More broadly, these combined characterization tools should provide insight into natural melanins and, therefore, any potential differences or similarities between their various forms and their synthetically accessible mimics.

EXPERIMENTAL SECTION

Particle Synthesis and Characterization

All chemicals were purchased from Sigma-Aldrich and used without further purification. SMNP-0 and SMNP-1 were prepared according to a literature method.[15]

General synthetic method for SMNP-i (i = 2, 3, 4, 5) (prepolymerization doping strategy): 45 mg of dopamine hydrochloride and different amounts of iron(III) chloride hexahydrate were fully dissolved in 130 mL of deionized water under stirring at room temperature for 1 h. Subsequently, 20 mL of Tris (2-amino-2-hydroxymethylpropane-1,3-diol) aqueous solution (with varying Tris concentrations, Table S1) was quickly injected into the established solution. It was observed that the solution color immediately turned red, gradually turning black after 0.5 h. After another 1.5 h, the targeted SMNP-i was separated by centrifugation and washed three times with deionized water.

TEM was performed on a FEI Sphera microscope operating at 200 keV. TEM grids were prepared by depositing small (3.5 μL) aliquots of sample onto grids (~2 min, Formvar stabilized with carbon (5–10 nm) on 400 copper mesh, Ted Pella Inc.) that had previously been glow discharged using an Emitech K350 glow discharge unit and plasma-cleaned for 90 s in an E.A. Fischione 1020 unit. Micrographs were recorded on a 2 K × 2 K Gatan CCD camera.

Cryo-TEM experiments were also performed on a FEI Sphera microscope operating at 200 keV. TEM grids were prepared by depositing small (3.5 μL) aliquots of sample onto grids (Quantifoil R2/2 holey carbon) that had previously been glow discharged using an Emitech K350 glow discharge unit and plasma-cleaned for 90 s in an E.A. Fischione 1020 unit. Samples were loaded onto the grids at 4 °C, blotted with filter paper to create a thin film on the grid, plunged into liquid ethane, and transferred into a precooled Gatan 626 cryo-transfer holder, which maintained the specimen at liquid-nitrogen temperature in a FEI Sphera microscope operated at 200 kV. Micrographs were recorded on a 2 K × 2 K Gatan CCD camera.

STEM and STEM-EDS analyses were acquired on a JEOL JEM 2100F TEM equipped with an INCA (Oxford) EDS detector at the NanoScale Fabrication and Characterization Facility, Peterson Institute of Nanoscience and Engineering, University of Pittsburgh, PA. Samples were prepared by drop-casting 5 μL of sample onto TEM grids (ultrathin 5 nm A-type carbon with 400 mesh copper, Ted Pella, Inc.) followed by slow drying while covered on the benchtop for at least 3 h. Samples were then dried under vacuum for 24–48 h to remove contamination that would interfere with STEM-EDS. Grids were loaded into a JEOL 31640 beryllium double-tilt holder. STEM-EDS data were collected for 180–600 s at specific points, using the largest probe size (1.5 nm electron beam diameter) with a 200 kV accelerating voltage. Images were collected in bright field and HAADF modes.

SEM images were acquired on a FEI XL ESEM-FEG (FEI Company) with a mica substrate. Samples were fully dried under vacuum for 12 h before the testing.

UV–vis spectra were obtained by using a PerkinElmer Lambda 35 UV/vis spectrophotometer.

Determination of Fe(III) Concentration

In order to determine Fe(III) concentration, the metal was first stripped from the synthetic melanin particles using the following procedure. To an aliquot of each sample (100 μL) was added 1% HNO_3 in water (1900 μL). Each mixture was then stirred for 12 h. The Fe(III) concentration was then quantified by inductively coupled plasma-optical emission spectrometry (ICP-OES) using a PerkinElmer Optima 3000DV spectrometer in the Scripps Institution of Oceanography, University of California, San Diego, CA.

SQUID Measurements

The magnetic properties of SMNP were characterized using a Quantum Design MPMS3 SQUID with a maximum field of 7 T. Freeze-dried solid samples (~10 mg) were packed into standard Quantum Design plastic sample holders. Magnetization data were collected in dc

mode and corrected for diamagnetic contributions using Pascal's constants. The axial anisotropy parameter D was fitted by the MagProp module in DAVE 2.3.[50]

EPR Experiments

Spectra in the range of 125 to 320 K were acquired on a Bruker Elexsys 580 spectrometer equipped with an SHQE resonator and a Bruker continuous flow liquid nitrogen cryostat. Spectra at temperatures between 3.5 and 125 K were acquired on a Bruker EMX spectrometer using an ER 4116DM dual-mode resonator and an Oxford ESR910 helium continuous flow cryostat. Liquid samples for frozen solution experiments were loaded in 4 mm o.d. × 3 mm i.d. FEP tubes (Wilmad). Room-temperature liquid samples were contained in 1.8 mm o.d. × 1 mm i.d. Teflon tubing (McMaster-Carr), while powder samples were contained in traditional 4 mm o.d. × 3 mm i.d. quartz tubes (Wilmad). Microwave frequency was typically ~9.34 GHz (SHQE resonator) with a power of 20 mW. The field was swept from 0 to 8000 G in 168 s and modulated at a frequency of 100 kHz with 20 G amplitude. A time constant of 82 ms was employed.

^1H NMRD Measurements

Proton $1/T_1$ NMRD profiles were measured on a fast field-cycling Stelar SMARTracer Relaxometer (Stelar, Mede (PV), Italy) at magnetic field strengths from 0.00024 to 0.25 T (corresponding to 0.01–10 MHz proton Larmor frequencies) at room temperature. The relaxometer operates under computer control with an absolute uncertainty in $1/T_1$ of ±1%. Additional data points in the range 15–70 MHz were obtained on a Bruker WP80 NMR electromagnet adapted to variable-field measurements (15–80 MHz proton Larmor frequency) on a Stelar Relaxometer. The $_1H$ T_1 relaxation times were acquired by the standard inversion recovery method with a typical 90° pulse width of 3.5 μs, 16 experiments of 4 scans. The temperature was controlled with a Stelar VTC-91 airflow heater equipped with a calibrated copper–constantan thermocouple (uncertainty of ±0.1 °C).

Fe(III) Stability in PBS

To determine the stability of Fe(III) chelated in SMNP-i (i = 2–5), we redispersed these two types of micellar nanoparticles in PBS (pH = 7.4). A 300 μL amount of SMNP-i (i = 2–5) solution (three replicates) was added in 500 μL dialysis tubes with M_w = 10 000, respectively, and dialyzed to 500 mL of PBS (pH = 7.4) under room temperature with magnetic stirring. Then 20 μL SMNP-i (i = 2–5) aliquots were taken at time points of 8 h, 24 h, 48 h, 72 h, and 7 days for ICP-OES analysis.

MR Imaging Measurements

The MR images were acquired on a Bruker 7.0 T magnet with Avance II hardware equipped with a 72 mm quadrature transmit/receive coil. T_1 contrast was determined by selecting regions of interest using the software ParaVision version 5.1. The parameters for 7 T MRI are T_R = 750.0 ms, T_E = 12.6 ms, echo = 1/1, FOV = 6.91/3.12 cm, slice thickness = 2 mm, nex = 2 mm, matrix = 256 × 116.

Supplementary Material

Refer to Web version on PubMed Central for supplementary material.

Acknowledgments

REFERENCES

1. d'Ischia M, Napolitano A, Ball V, Chen C-T, Buehler MJ. Polydopamine and Eumelanin: From Structure–Property Relationships to a Unified Tailoring Strategy. Acc. Chem. Res. 2014; 47:3541–3550. [PubMed: 25340503]

2. Ju K-Y, Lee Y, Lee S, Park SB, Lee J-K. Bioinspired Polymerization of Dopamine to Generate Melanin-Like Nanoparticles Having an Excellent Free-Radical-Scavenging Property. Biomacromolecules. 2011; 12:625–632. [PubMed: 21319809]

3. Liu Y, Ai K, Lu L. Polydopamine and Its Derivative Materials: Synthesis and Promising Applications in Energy, Environmental, and Biomedical Fields. Chem. Rev. 2014; 114:5057–5115. [PubMed: 24517847]

4. Ai K, Liu Y, Ruan C, Lu L, Lu GM. Sp^2 C-Dominant N-Doped Carbon Sub-Micrometer Spheres with a Tunable Size: A Versatile Platform for Highly Efficient Oxygen-Reduction Catalysts. Adv. Mater. 2013; 25:998–1003. [PubMed: 23239109]

5. Ma S, Liu L, Bromberg V, Singler TJ. Electroless Copper Plating of Inkjet-Printed Polydopamine Nanoparticles: a Facile Method to Fabricate Highly Conductive Patterns at Near Room Temperature. ACS Appl. Mater. Interfaces. 2014; 6:19494–19498. [PubMed: 25360833]

6. Ma S, Liu L, Bromberg V, Singler TJ. Fabrication of Highly Electrically Conducting Fine Patterns via Substrate-Independent Inkjet Printing of Mussel-Inspired Organic Nano-Material. J. Mater. Chem. C. 2014; 2:3885–3889.

7. Liu Y, Ai K, Liu J, Deng M, He Y, Lu L. Dopamine-Melanin Colloidal Nanospheres: An Efficient Near-Infrared Photothermal Therapeutic Agent for In Vivo Cancer Therapy. Adv. Mater. 2013; 25:1353–1359. [PubMed: 23280690]

8. Stritzker J, Kirscher L, Scadeng M, Deliolanis NC, Morscher S, Symvoulidis P, Schaefer K, Zhang Q, Buckel L, Hess M, et al. Vaccinia Virus-mediated Melanin Production Allows MR and Optoacoustic Deep Tissue Imaging and Laser-Induced Thermotherapy of Cancer. Proc. Natl. Acad. Sci. U. S. A. 2013; 110:3316–3320. [PubMed: 23401518]

9. Xiao M, Li Y, Allen MC, Deheyn DD, Yue X, Zhao J, Gianneschi NC, Shawkey MD, Dhinojwala A. Bio-Inspired Structural Colors Produced via Self-Assembly of Synthetic Melanin Nanoparticles. ACS Nano. 2015; 9:5454–5460. [PubMed: 25938924]

10. Xiao M, Li Y, Zhao J, Wang Z, Gao M, Gianneschi NC, Dhinojwala A, Shawkey MD. Stimuli-Responsive Structurally Colored Films from Bioinspired Synthetic Melanin Nanoparticles. Chem. Mater. 2016; 28:5516–5521.

11. Krogsgaard M, Behrens MA, Pedersen JS, Birkedal H. Self-Healing Mussel-Inspired Multi-pH-Responsive Hydrogels. Biomacromolecules. 2013; 14:297–301. [PubMed: 23347052]

12. Li L, Smitthipong W, Zeng H. Mussel-Inspired Hydrogels for Biomedical and Environmental Applications. Polym. Chem. 2015; 6:353–358.

13. Guo L, Liu Q, Li G, Shi J, Liu J, Wang T, Jiang G. A Mussel-Inspired Polydopamine Coating as a Versatile Platform for the In Situ Synthesis of Graphene-Based Nanocomposites. Nanoscale. 2012; 4:5864–5867. [PubMed: 22945453]

14. Ang JM, Du Y, Tay BY, Zhao C, Kong J, Stubbs LP, Lu X. One-Pot Synthesis of Fe(III)-Polydopamine Complex Nanospheres: Morphological Evolution, Mechanism, and Application of

the Carbonized Hybrid Nanospheres in Catalysis and Zn-Air Battery. Langmuir. 2016; 32:9265–9275. [PubMed: 27550631]

15. Ju K-Y, Lee JW, Im GH, Lee S, Pyo J, Park SB, Lee JH, Lee J-K. Bio-Inspired, Melanin-Like Nanoparticles as a Highly Efficient Contrast Agent for T_1-Weighted Magnetic Resonance Imaging. Biomacromolecules. 2013; 14:3491–3497. [PubMed: 23987128]

16. Miao Z-H, Wang H, Yang H, Li Z-L, Zhen L, Xu C-Y. Intrinsically Mn^{2+}-Chelated Polydopamine Nanoparticles for Simultaneous Magnetic Resonance Imaging and Photothermal Ablation of Cancer Cells. ACS Appl. Mater. Interfaces. 2015; 7:16946–16952. [PubMed: 26196160]

17. Borg DC. Transient Free Radical Forms of Hormones: EPR Spectra from Catecholamines and Adrenochrome. Proc. Natl. Acad. Sci. U. S. A. 1965; 53:633–639. [PubMed: 14338245]

18. Sever MJ, Weisser JT, Monahan J, Srinivasan S, Wilker JJ. Metal-Mediated Cross-Linking in the Generation of a Marine-Mussel Adhesive. Angew. Chem., Int. Ed. 2004; 43:448–450.

19. Weisser JT, Nilges MJ, Sever MJ, Wilker JJ. EPR Investigation and Spectral Simulations of Iron-Catecholate Complexes and Iron–Peptide Models of Marine Adhesive Cross-Links. Inorg. Chem. 2006; 45:7736–7747. [PubMed: 16961365]

20. Burlamacchi L, Lai A, Monduzzi M, Saba G. NMR, EPR, and INDO Studies on the Complexes of Dopamine with Cu^{2+}, Mn^{2+}, and Fe^{3+} in Aqueous Solution. J. Magn. Reson. 1983; 55:39–50.

21. Lucarini M, Pedulli GF, Guerra M. A Critical Evaluation of the Factors Determining the Effect of Intramolecular Hydrogen Bonding on the O-H Bond Dissociation Enthalpy of Catechol and of Flavonoid Antioxidants. Chem. - Eur. J. 2004; 10:933–939. [PubMed: 14978819]

22. Bolzoni F, Giraudo S, Lopiano L, Bergamasco B, Fasano M, Crippa PR. Magnetic Investigations of Human Mesencephalic Neuromelanin. Biochim. Biophys. Acta, Mol. Basis Dis. 2002; 1586:210–218.

23. Aime S, Bergamasco B, Biglino D, Digilio G, Fasano M, Giamello E, Lopiano L. EPR Investigations of the Iron Domain in Neuromelanin. Biochim. Biophys. Acta, Mol. Basis Dis. 1997; 1361:49–58.

24. Gerlach M, Trautwein AX, Zecca L, Youdim MBH, Riederer P. Mossbauer Spectroscopic Studies of Purified Human Neuromelanin Isolated From the Substantia Nigra. J. Neurochem. 1995; 65:923–926. [PubMed: 7616255]

25. Charkoudian LK, Franz KJ. Fe(III)-Coordination Properties of Neuromelanin Components: 5,6-Dihydroxyindole And 5,6-Dihydroxyindole-2-Carboxylic Acid. Inorg. Chem. 2006; 45:3657–3664. [PubMed: 16634598]

26. Della Vecchia NF, Luchini A, Napolitano A, Derrico G, Vitiello G, Szekely N, Dischia M, Paduano L. Tris Buffer Modulates Polydopamine Growth, Aggregation, and Paramagnetic Properties. Langmuir. 2014; 30:9811–9818. [PubMed: 25066905]

27. Koenig SH, Brown RD, Spiller M, Chakrabarti B, Pande A. Intermolecular Protein Interactions in Solutions of Calf lens Alpha-Crystallin. Results from $1/T_1$ Nuclear Magnetic Relaxation Dispersion Profiles. Biophys. J. 1992; 61:776–785. [PubMed: 1504248]

28. Aime S, Botta M, Terreno E. Gd(III)-Based Contrast Agents for MRI. Adv. Inorg. Chem. 2005; 57:173–237.

29. Bertini I, Luchinat C, Parigi G. Chapter 5 Transition Metal Ions: Shift and Relaxation. Curr. Methods Inorg. Chem. 2001; 2:143–203.

30. Bertini I, Capozzi F, Luchinat C, Xia Z. Nuclear and Electron Relaxation of Hexaaquairon^{3+} J. Phys. Chem. 1993; 97:1134–1137.

31. Bertini I, Galas O, Luchinat C, Messori L, Parigi G. A Theoretical Analysis of the ^{1}H Nuclear Magnetic Relaxation Dispersion Profiles of Diferric Transferrin. J. Phys. Chem. 1995; 99:14217–14222.

32. Bertini I, Luchinat C, Nerinovski K, Parigi G, Cross M, Xiao Z, Wedd AG. Application of NMRD to Hydration of Rubredoxin and a Variant Containing a $(Cys-S)_3Fe^{III}(OH)$ Site. Biophys. J. 2003; 84:545–551. [PubMed: 12524306]

33. Koenig SH, Brown RD, Lindstrom TR. Interactions of Solvent with the Heme Region of Methemoglobin and Fluoro-Methemoglobin. Biophys. J. 1981; 34:397–408. [PubMed: 6264989]

34. Li Y, Huang Y, Wang Z, Carniato F, Xie Y, Patterson JP, Thompson MP, Andolina CM, Ditri TB, Millstone JE, et al. Polycatechol Nanoparticle MRI Contrast Agents. Small. 2016; 12:668–677. [PubMed: 26681255]

35. Sitbon G, Bouccara S, Tasso M, Francois A, Bezdetnaya L, Marchal F, Beaumont M, Pons T. Multimodal Mn-Doped I-III-VI Quantum Dots for Near Infrared Fluorescence and Magnetic Resonance Imaging: from Synthesis to *in vivo* Application. Nanoscale. 2014; 6:9264–9272. [PubMed: 24980473]

36. Fan Q, Cheng K, Hu X, Ma X, Zhang R, Yang M, Lu X, Xing L, Huang W, Gambhir SS, Cheng Z. Transferring Biomarker into Molecular Probe: Melanin Nanoparticle as a Naturally Active Platform for Multimodality Imaging. J. Am. Chem. Soc. 2014; 136:15185–15194. [PubMed: 25292385]

37. Vitiello G, Pezzella A, Zanfardino A, Varcamonti M, Silvestri B, Costantini A, Branda F, Luciani G. Titania as a Driving Agent for DHICA Polymerization: a Novel Strategy for the Design of Bioinspired Antimicrobial Nanomaterials. J. Mater. Chem. B. 2015; 3:2808–2815.

38. Sarna T, Hyde JS, Swartz HM. Ion Exchange in Melanin: an Electron Spin Resonance Study with Lanthanide Probes. Science. 1976; 192:1132–1134. [PubMed: 179142]

39. Rabenstein MD, Shin Y-K. Determination of the Distance Between Two Spin Labels Attached to a Macromolecule. Proc. Natl. Acad. Sci. U. S. A. 1995; 92:8239–8243. [PubMed: 7667275]

40. Sebby KB, Walter ED, Usselman RJ, Cloninger MJ, Singel DJ. End-Group Distributions of Multiple Generations of Spin-Labeled PAMAM Dendrimers. J. Phys. Chem. B. 2011; 115:4613–4620. [PubMed: 21469686]

41. Usselman RJ, Russek SE, Klem MT, Allen MA, Douglas T, Young M, Idzerda YU, Singel DJ. Temperature Dependence of Electron Magnetic Resonance Spectra of Iron Oxide Nanoparticles Mineralized in Listeria Innocua Protein Cages. J. Appl. Phys. 2012; 112:084701.

42. Grillo VA, Hanson GR, Wang D, Hambley TW, Gahan LR, Murray KS, Moubaraki B, Hawkins CJ. Synthesis, X-ray Structural Determination, and Magnetic Susceptibility, Mössbauer, and EPR Studies of $(Ph_4P)_2[Fe_2(Cat)_4(H_2O)_2]\cdot 6H_2O$, a Catecholato-Bridged Dimer of Iron(III). Inorg. Chem. 1996; 35:3568–3576.

43. Anderson BF, Web J, Buckingham DA, Robertson GB. Crystal and Molecular Structure of Piperidinium μ-Acetato-di-μ-1,2-benzenediolato-bis-1,2-benzenediolatoferrate(III), $(C_5H_{12}N)_3$ $[(CH_3COO)\{Fe(C_6H_4O_2)_2\}_2]$: A Compound of Relevance to the 2Fe-Active Site of the Respiratory Protein Hemerythrin. J. Inorg. Biochem. 1982; 16:21–32.

44. Ainscough EW, Brodie AM, McLachlan SJ, Brown KL. The Reaction of 1,1′-biphenyl-2,2′-dial with Iron(III) and the Crystal Structure of Piperidinium Bis[μ-(1,1′-biphenyl-2,2′-diolato-O, μ-O′)-(1,1′-biphenyl-2,2′-diolato-O,O′)ferrate(III)]-ethanol(1/2). J. Chem. Soc., Dalton Trans. 1983:1385–1389.

45. Fisher OZ, Larson BL, Hill PS, Graupner D, Nguyen-Kim M-T, Kehr NS, De Cola L, Langer R, Anderson DG. Melanin-like Hydrogels Derived from Gallic Macromers. Adv. Mater. 2012; 24:3032–3036. [PubMed: 22566290]

46. Felix CC, Hyde JS, Sarna T, Sealy RC. Interactions of Melanin with Metal ions. Electron Spin Resonance Evidence for Chelate Complexes of Metal Ions with Free Radicals. J. Am. Chem. Soc. 1978; 100:3922–3926.

47. Gorun SM, Lippard SJ. Magnetostructural Correlations in Magnetically Coupled (μ-oxo)diiron(III) Complexes. Inorg. Chem. 1991; 30:1625–1630.

48. Taylor SW, Chase DB, Emptage MH, Nelson MJ, Waite JH. Ferric Ion Complexes of a DOPA-Containing Adhesive Protein from Mytilus Edulis. Inorg. Chem. 1996; 35:7572–7577.

49. Holten-Andersen N, Harrington MJ, Birkedal H, Lee BP, Messersmith PB, Lee KYC, Waite JH. pH-Induced Metal-Ligand Cross-Links Inspired by Mussel Yield Self-Healing Polymer Networks with Near-covalent Elastic Moduli. Proc. Natl. Acad. Sci. U. S. A. 2011; 108:2651–2655. [PubMed: 21278337]

50. Azuah RT, Kneller LR, Qiu Y. DAVE: A Comprehensive Software Suite for the Reduction, Visualization, and Analysis of Low Energy Neutron Spectroscopic Data. J. Res. Natl. Inst. Stand. Technol. 2009; 114:341–358. [PubMed: 27504233]

51. Sever MJ, Wilker JJ. Visible Absorption Spectra of Metal-Catecholate and Metal-Tironate Complexes. Dalton Trans. 2004:1061–1072. [PubMed: 15252685]

52. Prodi L, Rampazzo E, Rastrelli F, Speghini A, Zaccheroni N. Imaging Agents Based on Lanthanide Doped Nanoparticles. Chem. Soc. Rev. 2015; 44:4922–4952. [PubMed: 26090530]
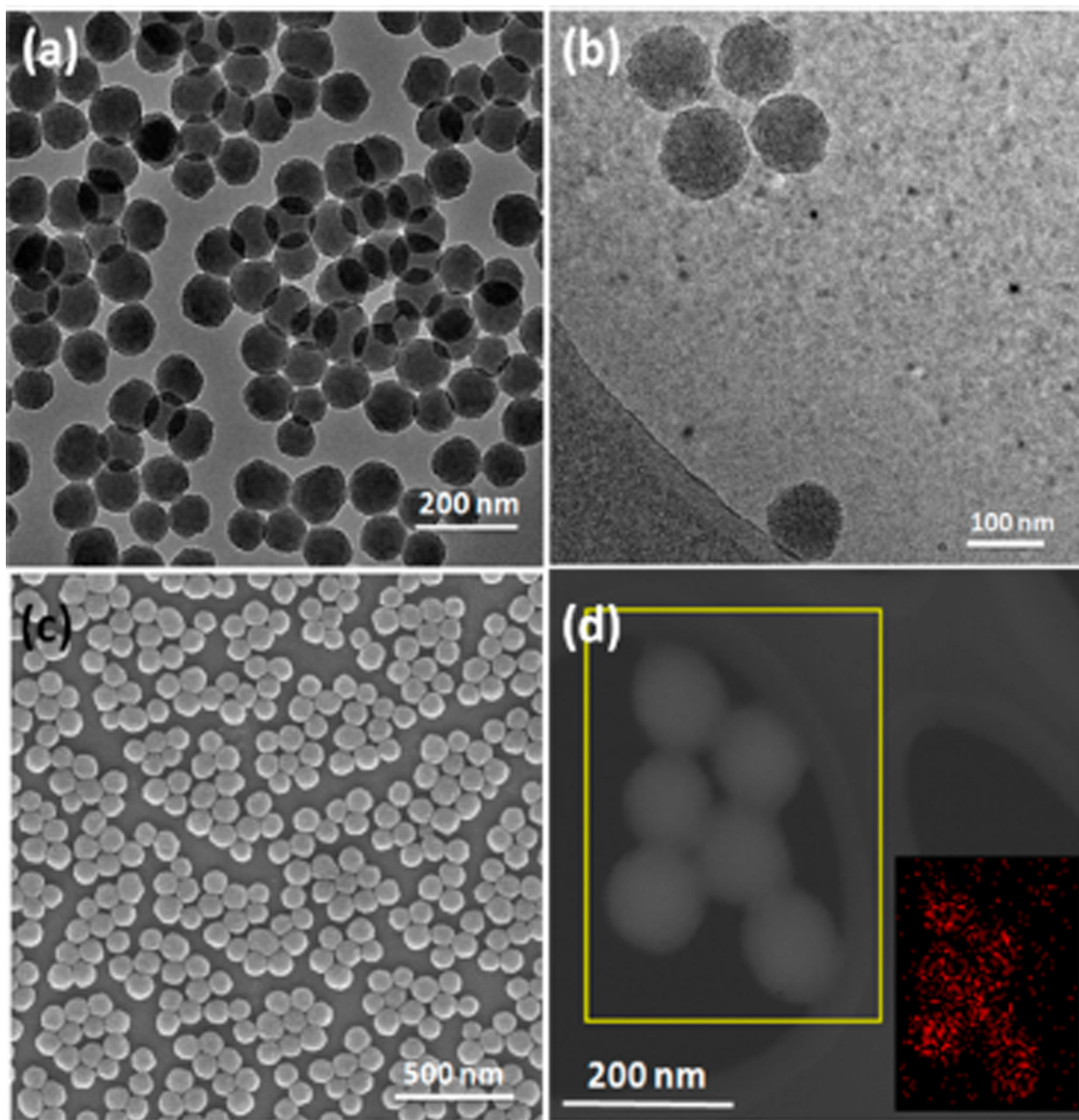
Figure 1.
Representative electron microscopy characterization of SMNP-4: (a) TEM; (b) cryo-TEM; (c) SEM; and (d) HAADF-STEM (inset is the selected area EDS Fe elemental mapping image).
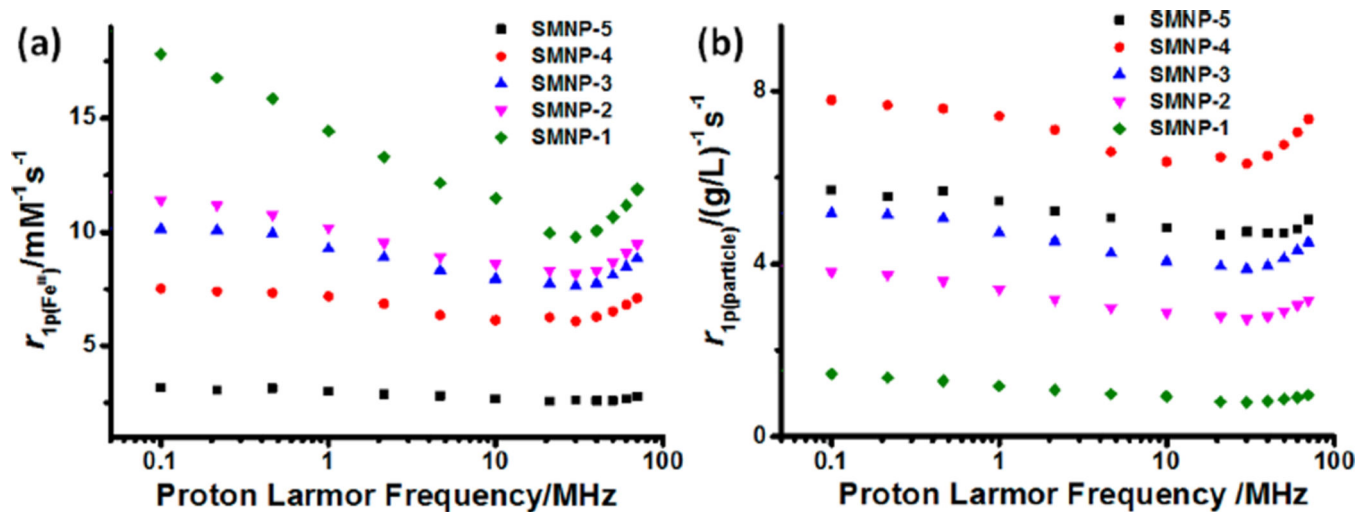
Figure 2.
(a) ^{1}H NMRD profiles for SMNP-i (i = 1–5). The x-axis is the proton Larmor frequency; the y-axis is the r_{1p} value per Fe(III) ion ($r_{1p(Fe(III))}$) for each SMNP. (b) ^{1}H NMRD profiles for SMNP-i (i = 1–5). The x-axis is the proton Larmor frequency; the y-axis is the r_{1p} value per SMNP ($r_{1p(particle)}$).
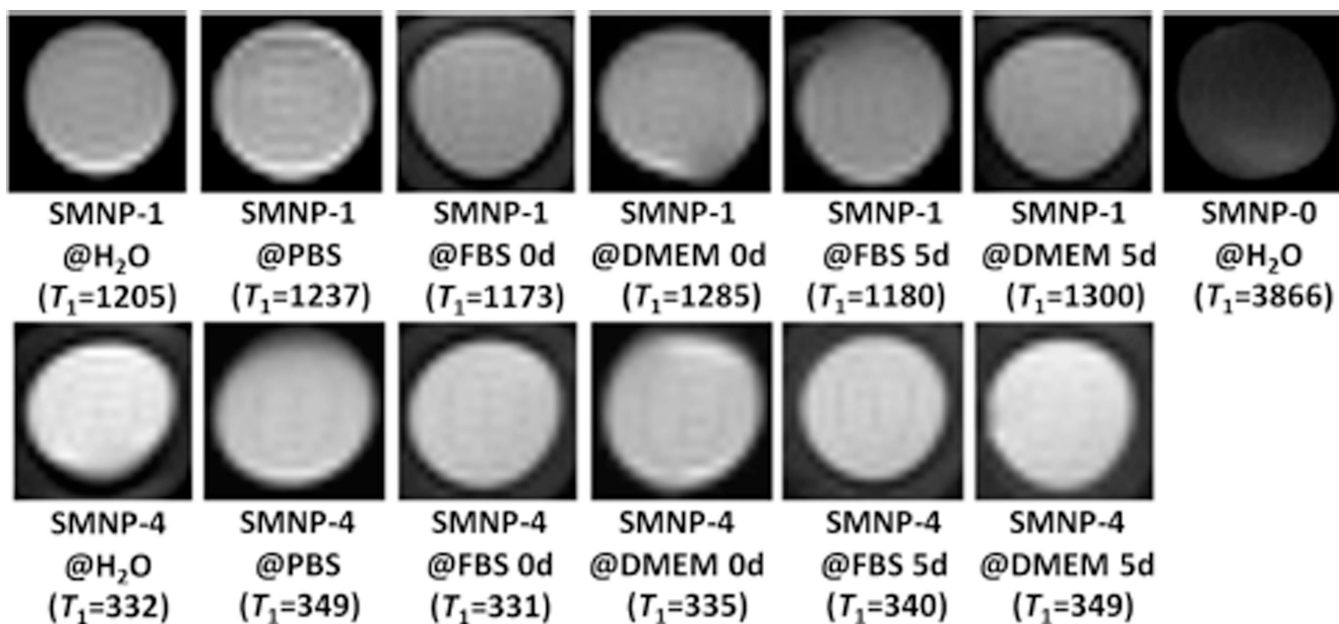
Figure 3.
T_1-weighted MR images captured on a Bruker 7.0 T magnet from SMNP-0, SMNP-1, and SMNP-4 in different media (particle concentration is 1.3 mg/mL in each tube). T_1 results for each phantom are shown below in milliseconds, respectively.
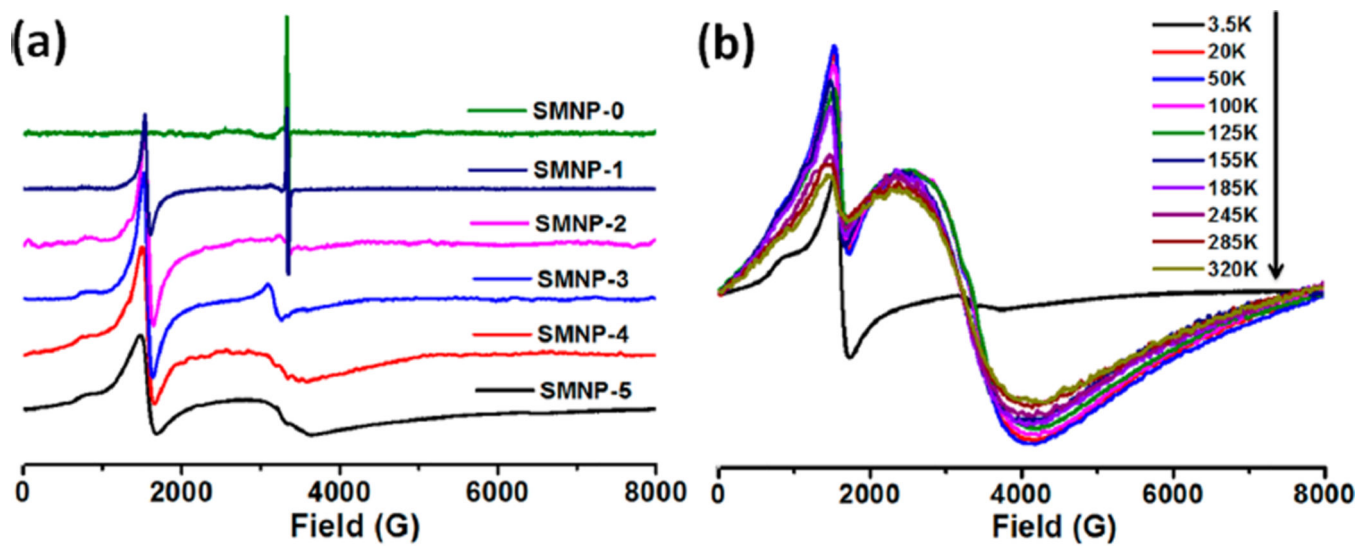
Figure 4.
(a) Experimental EPR spectra of SMNP-*i* (*i* = 0–5). (b) Temperature-dependent EPR analysis of SMNP-5.
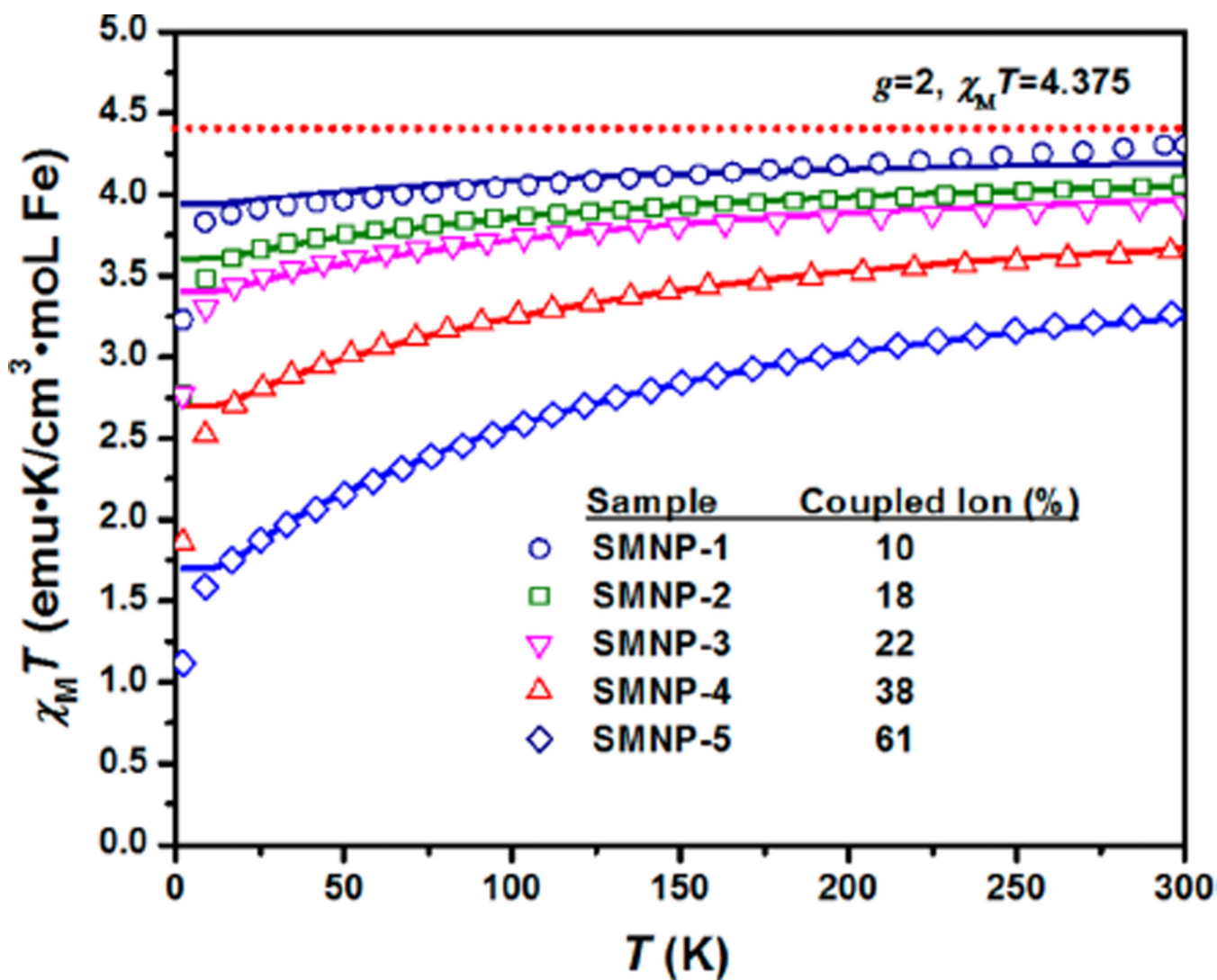
Figure 5.
Temperature dependence of the product of magnetic susceptibility and temperature ($\chi_M T$) for SMNP-i (i = 1–5). The dotted line describes the behavior of an isolated, isotropic Fe(III) ion. Solid lines represent a global fit of the data between 25 and 300 K as described in the text.
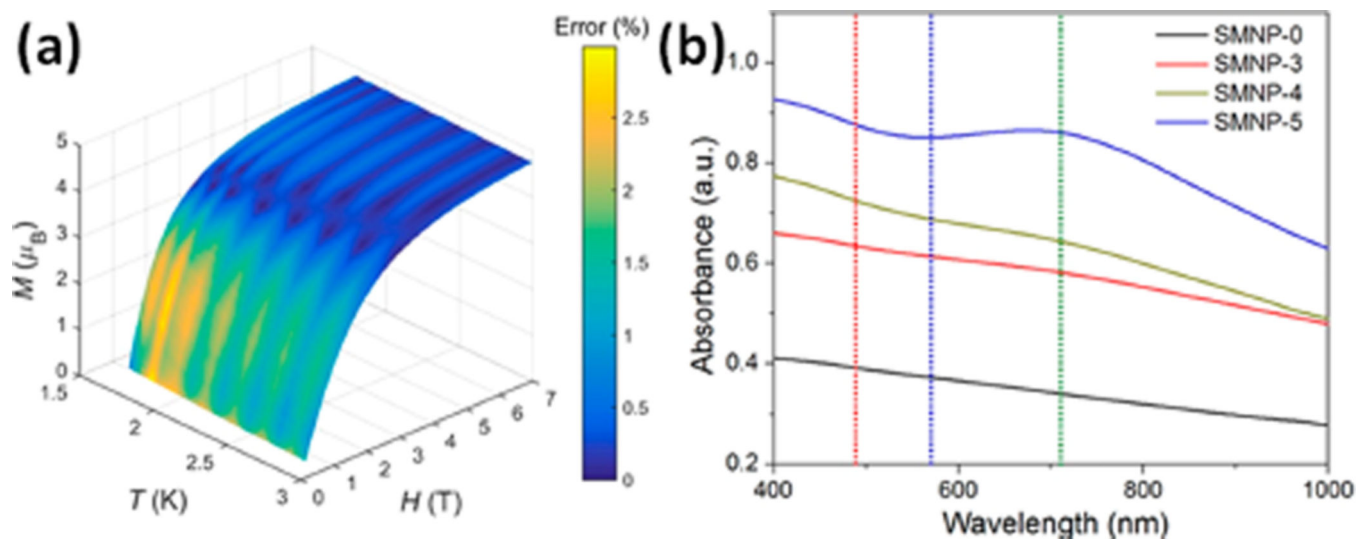
Figure 6.
(a) Plot of variable-temperature variable-field magnetization data for SMNP-1. The color bar represents the difference between experimental data and fitting results. A standard 2D M vs H/T plot is shown in Figure S9b. (b) UV–vis spectra of 0.1 mg/mL SMNP showing the transition from a featureless absorption for SMNP-0 to a well-defined yet broad structure in SMNP-5. Absorption peaks for mono- (~710 nm), bis- (~570 nm), and tris-catechol (~490 nm) are identified by dashed green, blue, and red lines, respectively.
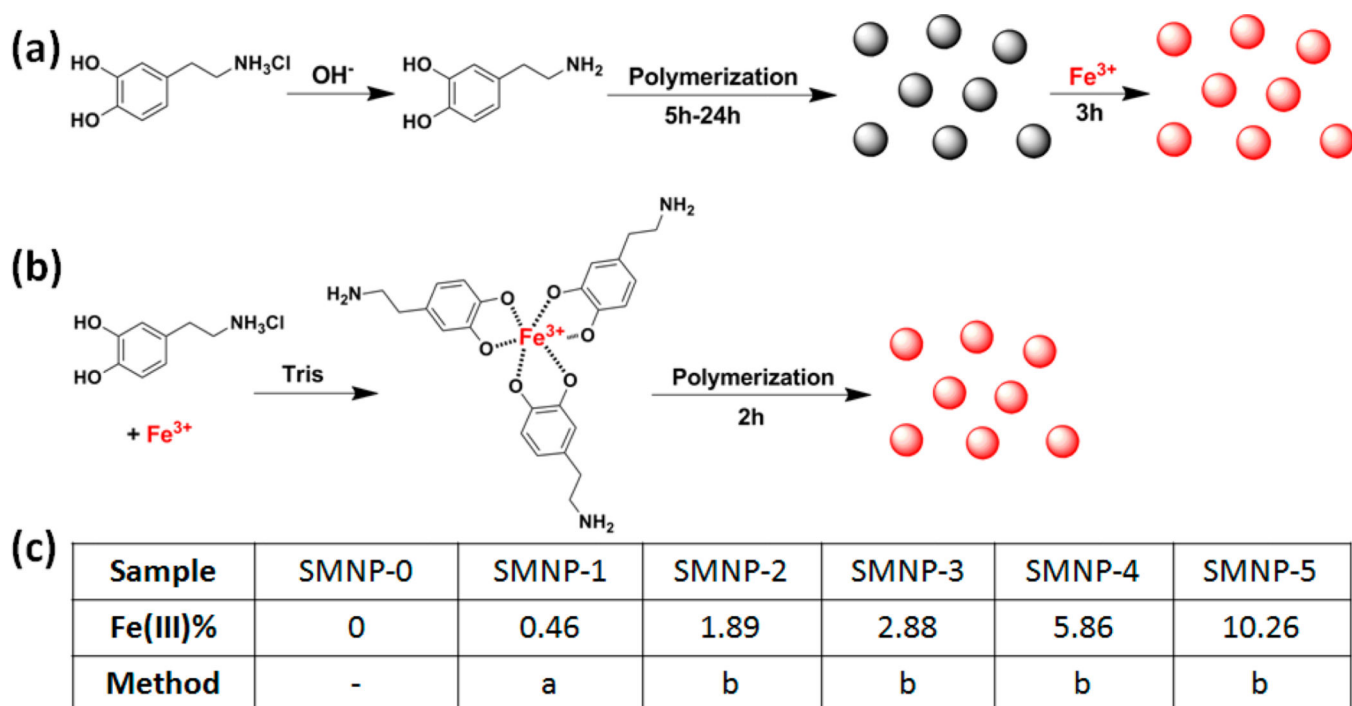
Scheme 1.
Preparation of SMNP-*i* (*i* = 0–5) samples: (a) postdoping strategy for SMNP-1, (b) prepolymerization doping strategy for SMNP-2, SMNP-3, SMNP-4, and SMNP-5, and (c) SMNP-*i* (*i* = 0–5) samples with different Fe(III) concentrations.